

# Fast wide-field photothermal and quantitative phase cell imaging with optical lock-in detection

Will J. Eldridge,<sup>1,2,\*</sup> Amihai Meiri,<sup>1,2,3</sup> Adi Sheinfeld,<sup>1</sup> Matthew T. Rinehart,<sup>1</sup>  
and Adam Wax<sup>1</sup>

<sup>1</sup>Department of Biomedical Engineering and Fitzpatrick Institute for Photonics, Duke University, Durham NC 27708, USA

<sup>2</sup>Equally contributing authors

<sup>3</sup>meiria1@gmail.com

\*wje4@duke.edu

**Abstract:** We present a fast, wide-field holography system for detecting photothermally excited gold nanospheres with combined quantitative phase imaging. An interferometric photothermal optical lock-in approach (POLI) is shown to improve SNR for detecting nanoparticles (NPs) on multiple substrates, including a monolayer of NPs on a silanized coverslip, and NPs bound to live cells. Furthermore, the set up allowed for co-registered quantitative phase imaging (QPI) to be acquired in an off-axis holographic set-up. An SNR of 103 was obtained for NP-tagging of epidermal growth factor receptor (EGFR) in live cells with a 3 second acquisition, while an SNR of 47 was seen for 20 ms acquisition. An analysis of improvements in SNR due to averaging multiple frames is presented, which suggest that residual photothermal signal can be a limiting factor. The combination of techniques allows for high resolution imaging of cell structure via QPI with the ability to identify receptor expression via POLI.

©2014 Optical Society of America

**OCIS codes:** (160.4236) Nanomaterials; (120.3180) Interferometry; (170.1650) Coherence imaging.

## References and links

1. S. Eustis and M. A. el-Sayed, "Why gold nanoparticles are more precious than pretty gold: noble metal surface plasmon resonance and its enhancement of the radiative and nonradiative properties of nanocrystals of different shapes," *Chem. Soc. Rev.* **35**(3), 209–217 (2006).
2. A. Wax, A. Meiri, S. Arumugam, and M. T. Rinehart, "Comparative review of interferometric detection of plasmonic nanoparticles," *Biomed. Opt. Express* **4**(10), 2166–2178 (2013).
3. A. Curry, W. L. Hwang, and A. Wax, "Epi-illumination through the microscope objective applied to darkfield imaging and microspectroscopy of nanoparticle interaction with cells in culture," *Opt. Express* **14**(14), 6535–6542 (2006).
4. N. A. Turko, A. Peled, and N. T. Shaked, "Wide-field interferometric phase microscopy with molecular specificity using plasmonic nanoparticles," *J. Biomed. Opt.* **18**(11), 111414 (2013).
5. C. Pache, N. L. Bocchio, A. Bouwens, M. Villiger, C. Berclaz, J. Goulley, M. I. Gibson, C. Santschi, and T. Lasser, "Fast three-dimensional imaging of gold nanoparticles in living cells with photothermal optical lock-in Optical Coherence Microscopy," *Opt. Express* **20**(19), 21385–21399 (2012).
6. S. Berciaud, L. Cognet, G. A. Blab, and B. Lounis, "Photothermal heterodyne imaging of individual nonfluorescent nanoclusters and nanocrystals," *Phys. Rev. Lett.* **93**(25), 257402 (2004).
7. A. Gaiduk, P. V. Rujigrok, M. Yorulmaz, and M. Orrit, "Detection limits in photothermal microscopy," *Chem. Sci.* **1**(3), 343–350 (2010).
8. E. Absil, G. Tessier, M. Gross, M. Atlan, N. Warnasooriya, S. Suck, M. Coppey-Moisan, and D. Fournier, "Photothermal heterodyne holography of gold nanoparticles," *Opt. Express* **18**(2), 780–786 (2010).
9. D. Boyer, P. Tamarat, A. Maali, B. Lounis, and M. Orrit, "Photothermal imaging of nanometer-sized metal particles among scatterers," *Science* **297**(5584), 1160–1163 (2002).
10. A. Datta, *Biological and Bioenvironmental Heat and Mass Transfer* (Marcel Dekker, 2002).
11. J. E. Mark, "Poly(dimethylsiloxane)," in *Polymer Data Handbook* (Oxford University Press, 1998).
12. J. D. Hoffman, *Numerical Methods for Engineers and Scientists, 2<sup>nd</sup> Ed.* (McGraw-Hill, 2001).
13. K. Seekell, M. J. Crow, S. Marinakos, J. Ostrander, A. Chilkoti, and A. Wax, "Hyperspectral molecular imaging of multiple receptors using immunolabeled plasmonic nanoparticles," *J. Biomed. Opt.* **16**(11), 116003 (2011).

14. K. Seekell, H. Price, S. Marinakos, and A. Wax, "Optimization of immunolabeled plasmonic nanoparticles for cell surface receptor analysis," *Methods* **56**(2), 310–316 (2012).
  15. M. C. Skala, M. J. Crow, A. Wax, and J. A. Izatt, "Photothermal optical coherence tomography of epidermal growth factor receptor in live cells using immunotargeted gold nanospheres," *Nano Lett.* **8**(10), 3461–3467 (2008).
  16. A. C. Curry, M.J. Crow, A. Wax, "Molecular imaging of epidermal growth factor receptor in live cells with refractive index sensitivity using dark-field microspectroscopy and immunotargeted nanoparticles," *J. Biomed. Opt.* **13**(1), 014022 (2008).
  17. M. J. Crow, G. Grant, J. M. Provenzale, and A. Wax, "Molecular imaging and quantitative measurement of epidermal growth factor receptor expression in live cancer cells using immunolabeled gold nanoparticles," *AJR Am. J. Roentgenol.* **192**(4), 1021–1028 (2009).
  18. M. J. Crow, K. Seekell, J. H. Ostrander, and A. Wax, "Monitoring of receptor dimerization using plasmonic coupling of gold nanoparticles," *ACS Nano* **5**(11), 8532–8540 (2011).
  19. M. J. Crow, S. M. Marinakos, J. M. Cook, A. Chilkoti, and A. Wax, "Plasmonic flow cytometry by immunolabeled nanorods," *Cytometry A* **79A**(1), 57–65 (2011).
  20. M. Atlan, M. Gross, P. Desbiolles, É. Absil, G. Tessier, and M. Coppey-Moisán, "Heterodyne holographic microscopy of gold particles," *Opt. Lett.* **33**(5), 500–502 (2008).
  21. A. Albanese, A.K. Lam, E.A. Sykes, J.V. Rocheleau, and W. C.W. Chan, "Tumour-on-a-chip provides an optical window into nanoparticle tissue transport," *Nat. Comm.* **4**, 1–8 (2013).
- 

## 1. Introduction

Due to their unique optical properties, plasmonic nanoparticles (NPs) have been utilized as labels for molecularly specific cell imaging. Plasmonic NPs exhibit a behavior known as localized surface plasmonic resonance (LSPR), where the electron cloud of the metal NP oscillates in response to an incident electromagnetic field, leading to E-field enhancements surrounding the NP at certain wavelengths. The spectral peak of the LSPR is dictated by the size, shape, and composition of the NP [1]. Multiple optical techniques have been established to detect NPs on multiple substrates [2]. These include, among others, dark-field microscopy [3], which takes advantage of enhanced NP scattering at their plasmonic resonance wavelength, and photothermal microscopy, which visualizes refractive index changes in the sample media due to localized NP heating [4–9]. One limitation of these approaches is that cellular structures are typically not visible. One recent study has demonstrated a wide-field photothermal imaging method which combined photothermal and phase images, but suffered from low signal to noise ratio (SNR) of the phase and photothermal signals [4].

To address the need for high SNR, Pache et. al demonstrated a photothermal imaging method in a heterodyne configuration to optically lock-in the photothermal signal of interest. The study demonstrated high SNR, but required long acquisition time due to the point-scanning approach [5]. This study did demonstrate cell imaging using dark field optical coherence microscopy (OCM), providing depth sectioning but not phase imaging. As an alternative method for combining the molecular specificity of labeled NPs with imaging of cellular features, we propose a wide-field photothermal optical lock-in system which incorporates a standard off-axis holography scheme. This approach greatly improves acquisition time compared to point-scanning photothermal methods as well as overcomes the poor SNR of the previous wide-field photothermal demonstration. This system provides high resolution quantitative phase information, coupled with a high SNR method for sensing the photothermal signals obtained from photothermally modulated NPs.

## 2. Background

The high absorption of plasmonic NPs at their plasmon resonance can be employed to locally heat the surrounding medium resulting in a refractive index change. Phase sensitive detection records the optical path length change due to this heating, enabling imaging of NPs.

When the excitation light is modulated by frequency  $\Omega$  the change in the refractive index of the medium can be described as:

$$\Delta n(r, t) = \frac{\partial n}{\partial T} \frac{P_{abs}}{4\pi\kappa r} \left[ 1 + \cos\left(\Omega t - \frac{r}{r_{th}}\right) e^{-r/r_{th}} \right] \quad (1)$$

where  $r$  is the distance from the particle,  $\partial n/\partial T$  is the variation of the refractive index of the medium with temperature,  $P_{abs}$  is the power absorbed by the NP,  $\kappa$  is the thermal conductivity of the surrounding medium, and  $r_{th} = [2\kappa/(\Omega C_p)]^{1/2}$  is the characteristic length for heat diffusion, which depends on the heat capacity per unit volume,  $C_p$  [6].

This phase change can be detected using a digital holography system, where a reference beam is interfered with a probe beam which passes through the sample. If these two arms are modulated at high frequency with a slight frequency shift  $\Omega$  between them, the result is a signal which is modulated at a beat frequency,  $\Omega$ . The detected intensity after Fourier filtering of the term of interest can be shown to be [5]

$$I(k, t) = E_i^2 T_n T_r^* e^{i(2kz_n + \Omega t)} e^{-i2kz_r} + E_i^2 T_{np} T_r^* e^{-i2kz_r} e^{i[k(2z_{np} + \alpha \cos(\Omega t)) + \Omega t]} \quad (2)$$

where  $E_i$  is the incident electric field amplitude,  $T_n$ ,  $T_r$ , and  $T_{np}$  are the sample, reference and NP transparency functions,  $z_n$ ,  $z_r$ , and  $z_{np}$  corresponds to axial position of the sample, reference, and NP field locations,  $\alpha$  is the induced optical path-length change, and  $k$  is the wavenumber of the probe and reference beams. Given an integration time of  $\Delta t = 2\pi m/\Omega$ , where  $m$  is an integer, the first term, corresponding to sample interference, goes to zero, leaving the second term as the optical lock-in term, corresponding to NP absorption. Integration of the second term over the same  $\Delta t$  results in a time-averaged signal of:

$$\langle I(k, t) \rangle = iE_i^2 T_{np} T_r^* e^{i2k(z_{np} - z_r)} \Delta t J_1(\alpha k) \quad (3)$$

where  $J_1$  is the first order Bessel function. This photothermal optical lock-in (POLI) detection scheme reveals the photothermal signal in  $T_{np}$  while eliminating the background phase signal where the NPs or the heating beam are absent.

In order to determine the SNR of our measurements, we also need to define the expected source of noise. For the signal in Eq. (3), the associated shot noise is:

$$\langle N(k, t) \rangle = \sqrt{\langle I(k, t) \rangle} = E_i \sqrt{T_{np} T_r^* \Delta t J_1(\alpha k)}. \quad (4)$$

Thus, the expected signal to noise ratio for signals where the integration time is an integer multiple of the modulation period is:

$$SNR = \langle I(k, t) \rangle / \langle N(k, t) \rangle = \sqrt{\langle I(k, t) \rangle} = E_i \sqrt{T_{np} T_r^* \Delta t J_1(\alpha k)}. \quad (5)$$

For a given nanoparticle configuration, characterized by  $T_{np}$  and  $\alpha$ , the ideal SNR scales as the square root of the integration time. For situations where the integration time is not an integer multiple of the modulation period, there is an additional source of noise, presented below in Eq. (6).

### 3. Methods

#### 3.1. Optical setup

An off-axis holography system was employed to detect the phase signal of the photothermally excited NPs (Fig. 1). Briefly, light from a 633 nm He-Ne laser (10mW) was split into probe and reference arms using a beamsplitter. Both arms were modulated ( $f = 110$  MHz) using acousto-optic modulators (1206C, Isomet) and a frequency synthesizer (IDDS2, Isomet). The reference field frequency was offset by  $\Omega$ , to allow for optical lock-in phase detection. Light transmitted through the sample was collected via a 40x objective (Leica 440 Achro, NA = 0.66) while the reference passed through another 40x objective (Leica 440 Achro, NA = 0.66)

and the two were combined. The resultant interference pattern was focused onto a monochrome CCD (Flea 3, Point Grey).

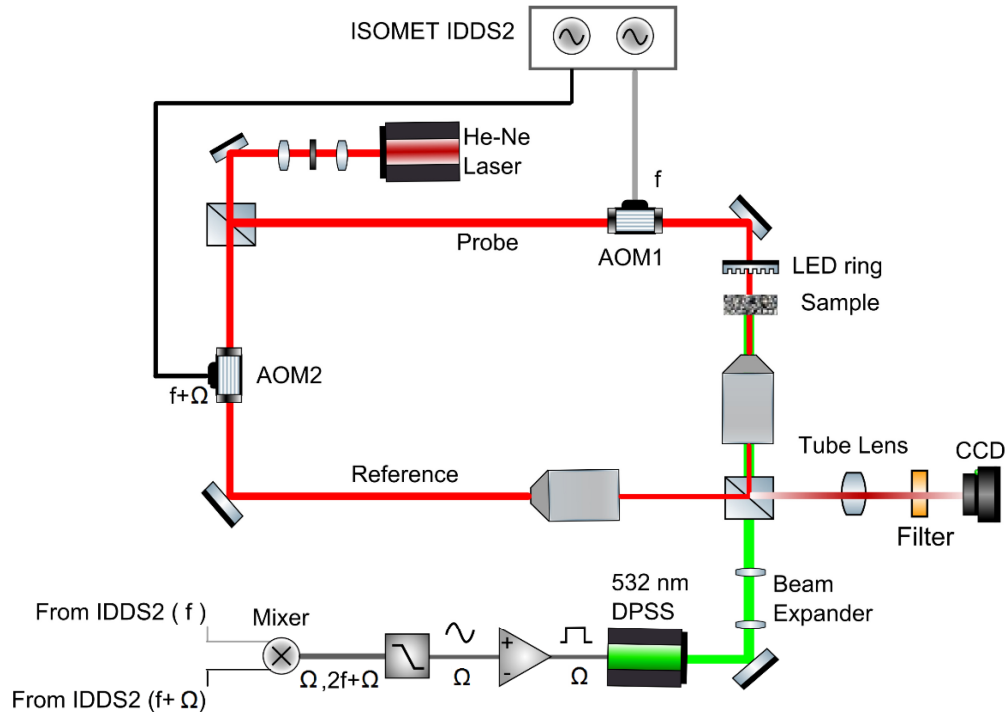


Fig. 1. Optical setup for the wide field optical lock-in detection scheme of gold NP labeled samples.

A square wave signal at the beat frequency,  $\Omega$ , was derived from the output of the IDDS-2 and used to modulate a 532 nm heating beam (C531005FX, Laserglow Technologies). To maximize absorption cross-section, 60 nm diameter gold NPs (15709-20, Ted Pella, Inc.) were used. The beam was focused onto the sample using the probe objective. A 532-nm notch filter (NF533-17, ThorLabs) was used to stop light from the heating beam from reaching the camera. The optical power of the heating beam at the sample was 18 mW. A dark-field LED ring (RL1360m, Advanced Illuminations) was used to visualize samples during alignment.

### 3.2. Data analysis

In off-axis holography, the reference field is overlapped with the sample field with a relative angle of propagation of 1 degree between them. The linear phase difference translates into a shift in the Fourier domain. Digital spatial filtering of the Fourier transform of the image allows for isolation of the interference term bearing information on the complex sample field. For the QPI or photothermal signals, the phase is extracted and unwrapped. In the case of photothermal signal, a reference frame, in which the heating beam is turned off, is subtracted. For the POLI images, the phase dependent complex amplitude, according to Eq. (3), is extracted by subtracting a dark frame to obtain a single frame photothermal signal. For each data set multiple frames were averaged to result in the final photothermal image. The implications of this averaging are examined below.

## 4. Results and discussion

### 4.1. Gold nanoparticle phantoms

A solution of 60 nm gold spheres with a concentration of  $1.8 \times 10^{11}$  NPs/mL was used to analyze both temporal and frequency dependence of the POLI signal SNR. The excitation beam was  $3\mu\text{m}$  diameter with 18mW power, corresponding to a heating intensity of  $250\text{ kW/cm}^2$ . The 3 micron heating beam was focused onto the nanoparticle sample, yielding a POLI signal that had a spatial extent corresponding to the thermal diffusion radius,  $r_{th}$ . Offset modulation frequencies ranged from 100 Hz to 1.1 kHz. The integration time was set to 50.013 ms, which was the closest integration time to an integer number of modulation periods allowed by the CCD hardware. The results in Fig. 2(a) show the SNR for different modulation frequencies based on a 10 frame average. Since the noise was independent of the modulation frequency, the SNR dependence could be estimated from Eq. (1) as  $\exp[-r/r_{th}]$  with  $r_{th}$  being proportional to  $1/\sqrt{\Omega}$ . Taking the thermal parameters of water,  $C_p = 4.18\text{ Jg}^{-1}\text{K}^{-1}$  and  $\kappa = 0.58\text{ Wm}^{-1}\text{K}^{-1}$  [10] and  $r = 10\mu\text{m}$ , based on the area for which the signal was averaged, yielded the theoretical curve shown in Fig. 2(a) which corresponded well with the experimental data.

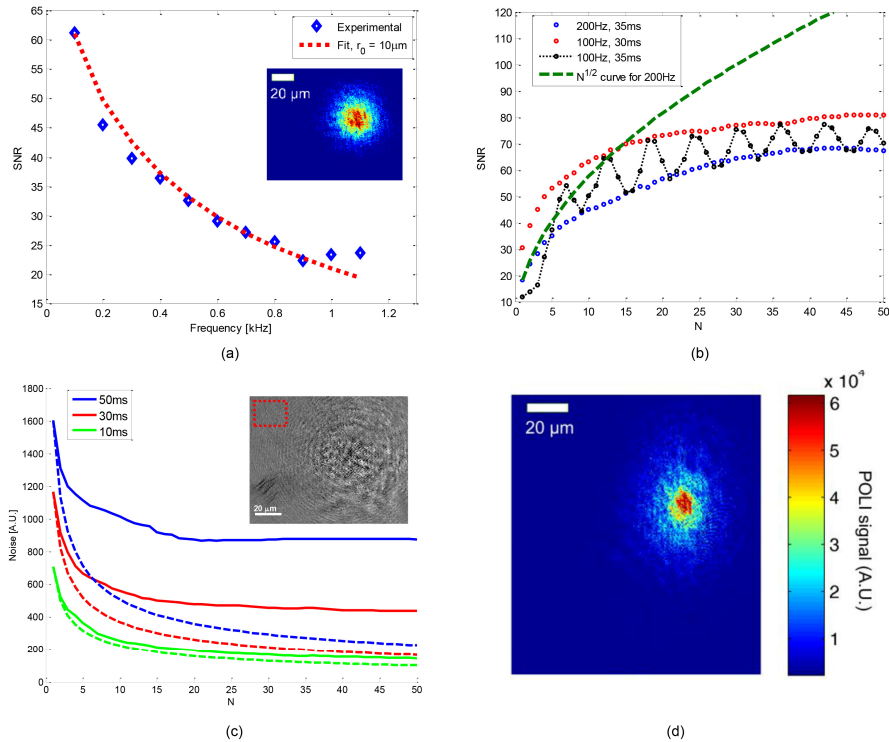


Fig. 2. (a) SNR of photothermal optical lock-in (POLI) signal averaged over 10 frames as a function of frequency for NPs in solution: experimental results (blue markers) and fit to the exponential decay of the thermally modulated refractive index profile, with  $r = 10\mu\text{m}$  (red dotted line). Inset: POLI signal for modulation frequency of 100Hz. (b) SNR as a function of number of averaged frames: modulation frequency of 100Hz at 30ms (red) and 35ms (black) integration times and 200Hz at 35 ms integration time (blue). For comparison, shot-noise limited  $\sqrt{N}$  dependence also shown (green dotted line), scaled to the first frame SNR value for the 200 Hz curve. (c) Noise as function of frames averaged for 100 Hz modulation frequency at different exposure times. The dotted lines show expected shot noise limited behavior. Inset: Modulated heat image minus no-heat image at 50ms exposure time and averaged over 50 frames, red rectangle marks the area taken for noise calculation. (d) POLI signal for a monolayer of NPs with a modulation of 100 Hz. The SNR obtained in this frame was 120.

Temporal dependence was analyzed by comparing SNR versus number of frames averaged for modulation frequency of 100Hz with exposure times of 30 and 35ms, and for 200Hz with an exposure time of 35 ms. The results, seen in Fig. 2(b), showed monotonic increase in SNR vs number of averaged frames when the exposure time was an integer number of modulation periods. However, when the exposure time was not an integer multiple of the modulation period the SNR trend was modulated with a sinusoidal pattern with the number of averaged frames. This can be explained by integrating Eq. (2) over the exposure time  $\Delta t = T_0 - \Delta t_N = 2\pi m/\Omega + \delta$ , where  $T_0$  is the start of the acquisition and  $\Delta t_N$  is the time delay between frames, which was not necessarily an integer of the modulation period. For the  $N^{\text{th}}$  frame, the noisy and undesired background which arises from the first term, equals:

$$B_N(k, t) = \text{Re} \left\{ E_i^2 T_n T_r^* e^{i2k(z_n - z_r)} \int_{T_0 N}^{T_0 N + \Delta t} e^{i\Omega t} dt \right\} \propto \frac{2}{\Omega} \cos[\Omega(\delta + \Delta t_N)N + \Omega\delta/2] \sin\left(\frac{\Omega\delta}{2}\right) \quad (6)$$

It can be seen that when  $\delta \neq 0$  this term produces a sinusoidal behavior versus the number of frames at a frequency defined both by the exposure time and by the delay between frames. Averaging frames 1 to  $N$  will still yield the same sinusoidal pattern. The integral over the second term in Eq. (2), representing the signal, does not have an analytical solution, however it also includes a sinusoidal term at a similar frequency when  $\delta \neq 0$ .

Figure 2(b) shows that the SNR increased almost according to  $\sqrt{N}$  when the number of averaged frames was smaller than 5. However, for a larger  $N$ , this trend significantly deviated from this behavior, reaching a saturation level for  $N > 30$ . Figure 2(c) shows the dependence of the noise alone with  $N$  at 100Hz for different values of exposure time, where all exposures were integers of the modulation period. The dotted lines show the  $(N\Delta t)^{-1/2}$  dependence that would have been expected had shot-noise been dominant, according to Eq. (4). From this figure it is clear that the noise deviated from this dependence when  $N$  increased, and this deviation increased with the exposure time. Since this noise increases with acquisition time, we deduced that this noise results from residual photothermal signal. This residual signal is can be seen in the image shown in the inset of Fig. 2(c), which was taken at 50ms exposure time and averaged over 50 frames. This noise sets a limitation on the SNR improvement that can be achieved via averaging frames in this system. For example, for an exposure time of 50ms there was almost no SNR improvement beyond 20 frames.

To demonstrate the potential of this POLI scheme to obtain high SNR images, images were acquired from 60 nm gold NPs immobilized on a silanized coverglass to form a monolayer. For this sample, glycerol-ethanol 50:50 was chosen as the photothermal medium, resulting in a peak SNR of 120, as shown in Fig. 2(d), as the photothermal media can compensate for the heat-sinking effect of a glass substrate [7]. Water proved to be a sufficient photothermal medium for NPs not directly bound to glass (i.e. NPs in suspension or bound to cells) but did not yield measurements with an SNR > 100.

To further illustrate the heat sinking properties of glass in photothermal microscopy, we imaged a solution of 60 nm gold NPs at a concentration of  $1 \cdot 10^{11}$  NPs/mL contained within a PDMS (polydimethylsiloxane) microchannel. Equation (3) shows that the photothermal signal, under a first order approximation of the Bessel function, is proportional to the induced optical path-length change  $\alpha$  and therefore is proportional to the change in the refractive index:  $\Delta n(r, t) = \Delta T(r, t) \cdot \partial n(r, t) / \partial T$ . Thus, differences in  $\partial n / \partial T$  can greatly affect the signal response. Figure 3(a) shows a POLI image ( $\Omega = 100\text{Hz}$ , 50ms exposure) where the beam illuminated the center of the channel. The beam was slightly defocused and the heating power was reduced in order to reduce the optical fluence and avoid damage to the PDMS. Upon comparing this image with a simulation of  $\Delta n(r)$ , good qualitative agreement was obtained.

The change in the refractive index was approximated using a finite-difference time-domain simulation of the heat propagation in a microchannel, multiplied by  $\partial n/\partial T$ . We used the value of  $\partial n/\partial T$  for PMMA (poly(methyl methacrylate)) [7], which is close to that of PDMS, given their similar composition. Thermal diffusivity of water and PDMS were taken to be  $1.43 \cdot 10^{-7}$  and  $1.06 \cdot 10^{-7}$  mm<sup>2</sup>/s, respectively [10,11]. Values of  $\partial n/\partial T$  for water and PDMS were estimated to be  $9 \cdot 10^{-5}$  K<sup>-1</sup> and  $1.2 \cdot 10^{-4}$  K<sup>-1</sup>, respectively. The simulation was performed in three dimensions, using the forward-time centered-space method [12], and a 2D simulated image was obtained at the z-plane at the center of the channel. The thermal diffusivity in PDMS is similar to the value in water, leading to similar propagation of the heat from the channel to the surrounding PDMS. However, the effect of the larger refractive index change in the PDMS leads to the image shown in Fig. 3(b), which resembles the experimental result. Since the simulation parameters were taken from the literature and not directly measured, only qualitative agreement is expected.

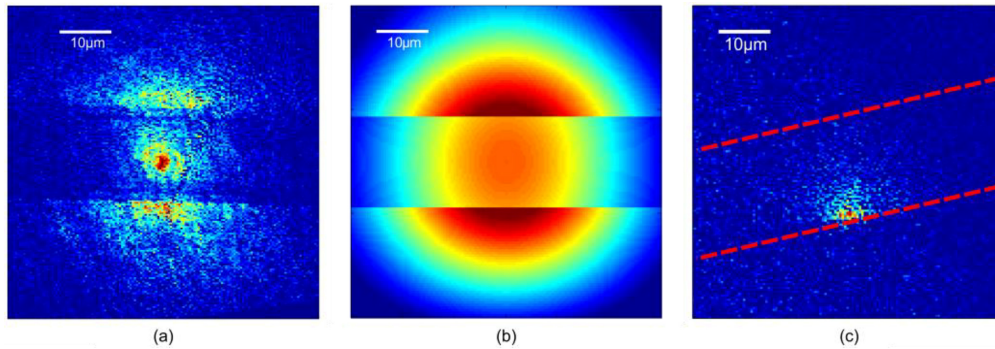


Fig. 3. (a) Photothermal optical lock-in (POLI) signal for a NP solution in a PDMS microchannel at a modulation frequency of 100Hz. (b) FDTD simulation of the change in the refractive index for a PDMS microchannel. (c) POLI signal for NPs solution in a glass microchannel (red dotted lines mark the channel edges, based on the phase image).

To confirm our findings, glass microchannels loaded with a similar NP solution were imaged (Fig. 3(c)). The beam illuminated the edge of the channel to highlight the interface between the two media. In this case, the coefficient of  $\partial n/\partial T$  in glass is more than 7 times smaller than in water [4], resulting in a signal confined to the channel. The SNR in this image was relatively low since the beam illuminated the channel edge and therefore only part of the beam interacted with the NPs.

#### 4.2. Biological cells

For imaging live cells, MDA-MB-468 cells were chosen for their high epidermal growth factor receptor (EGFR) expression [13], providing a good target for antibody conjugated NPs. For the cell sample preparation 0.5 mL of 60 nm gold NPs (15709-20, Ted Pella, Inc.) were diluted with 62.5 µL of 20mM HEPES buffer. 12 µL of anti-EGFR antibody (E2156, Sigma–Aldrich) was diluted with 488 µL of 20mM HEPES buffer. A 100 nM K<sub>2</sub>CO<sub>3</sub> solution was used to adjust the pH of each solution to  $7.0 \pm 0.2$ . The NP and antibody solutions were mixed on an oscillator for 20 min at 190 cycles/min. Following mixing, the resulting solution was tested for antibody-NP conjugation by adding 5µL of 10% NaCl to 100 µL of the solution. To prevent non-specific binding of proteins to the remaining NP surface, 100 µL of 1% Polyethylene glycol (PEG, P2263, Sigma–Aldrich) was added to the remaining 900 µL of the suspension and then allowed to interact for 10 min. 15 min of centrifuging (6000 RPM) was used to remove excess PEG. The supernatant was removed, and the NP pellet was resuspended with 0.5 mL of PBS. Approximately 80k MDA-MB-468 cells were plated on a chambered coverglass and incubated overnight. The cell media was removed and replaced by

0.5 mL PBS/5%FBS and 0.5 mL of antibody-NP solution. Following 20 minutes of incubation at 37 °C, the antibody-NP solution was removed, and cells were washed with media twice before imaging [13,14]. The same protocol was previously tested and validated by confirming anti-EGFR specific binding of nanoparticles to EGFR positive cancer cells with appropriate control experiments [3, 13–19]. Mie theory simulations indicate a substantially larger absorption cross section for 60 nm gold nanospheres as compared to lower diameter nanospheres, all of which have an absorption peak near 532 nm, the wavelength of the heating beam. Given the advantage of the higher absorption cross-section and the fact that EGFR is a cell surface receptor such that internalization is not required for labeling, 60 nm gold spheres were chosen over smaller diameter spheres for this work.

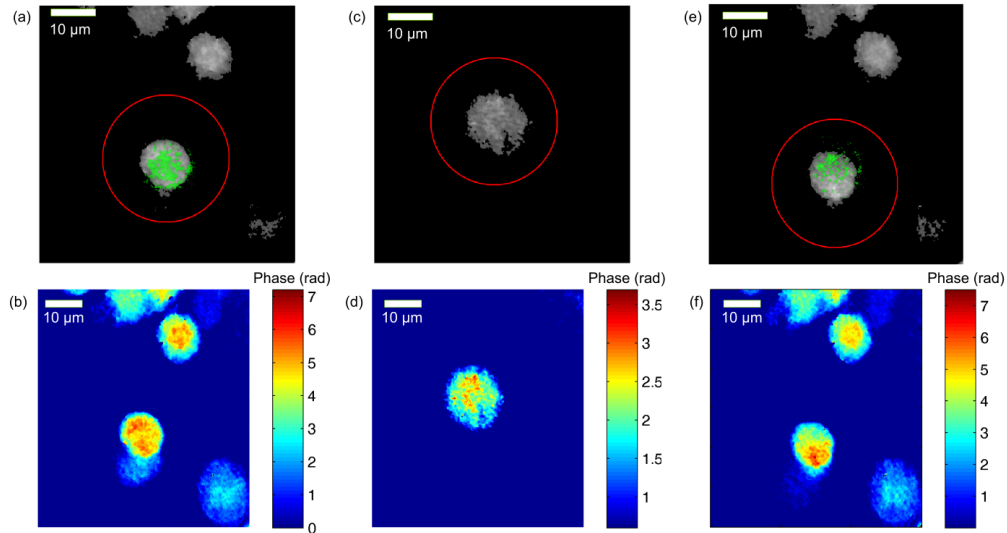


Fig. 4. MDA-MB-468 cell images. (a) Overlay of wide field POLI (green) and QPI grayscale images of NP tagged cell. The two images were normalized to 1 and then thresholded with values of 0.5, 0.3 for the POLI and QPI images respectively. Red circles mark the excitation beam location. (b) QPI image of the cell from (a). (c) and (d) Overlay image and QPI image of a negative control cell. (e) Overlay of POLI and QPI images for 20 ms total integration time. (f) QPI Image of the same cell in (e).

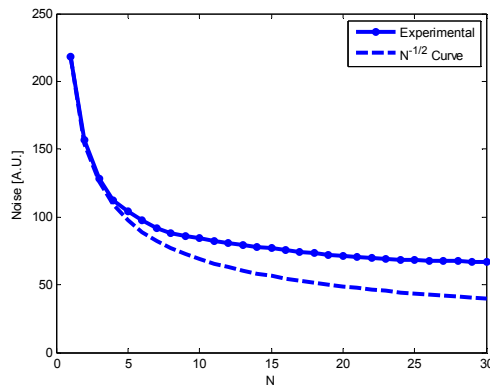


Fig. 5. Noise in POLI image as a function of frames averaged  $N$  for 100 Hz modulation frequency, with 50 ms integration time, using the data set seen in Fig. 4 (a). The dotted line shows expected shot noise limited behavior.

For cell imaging, the excitation beam was expanded to  $\sim 30 \mu\text{m}$  with 18 mW of excitation power, corresponding to a heating intensity of  $2.5 \text{ kW/cm}^2$ , and directed at the cells. The modulation frequency was 100 Hz and the integration time was  $\sim 50 \text{ ms}$ . Each POLI data set was composed of 30 image pairs, one with the heating beam modulated, and one with the heating beam disengaged. Thirty frames were chosen to achieve an SNR of around 100. A second set of images was recorded using 0 Hz offset frequency, yielding a QPI of the sample. The resultant images of NP tagged cells can be seen in Fig. 4(a), where the POLI signal (green) is overlaid with QPI (grayscale). Figure 4(b) shows the phase image of the same cells. This result showed good agreement between the POLI signal and the QPI, and a high SNR of 103 for the POLI data. The SNR improvement relative to the previous experiments on NPs in solution can be attributed to the heat confinement to the cells in addition to the longer averaging time. Furthermore, in the cell experiments, NPs bound to cells and are immobilized, unlike NPs in solution which can move freely during data acquisition, producing a larger signal. Figure 5 shows the noise dependence on the number of averaged frames for the POLI cell imaging. Compared to the results obtained from NPs in solution (Fig. 2(c)), the deviation from shot-noise expectation is significantly smaller due to the heat confinement to the cells, which effectively reduces the photothermal signal residue at the area used for noise calculation.

In order to confirm molecular specificity, cells which were not exposed to NPs were also imaged. The overlaid POLI and QPI images (Fig. 4(c)) agree with the phase only signal (Fig. 4(d)). To demonstrate the best acquisition speed of this method, the single frame exposure time was reduced to 10 ms corresponding to one period of heating excitation (100 Hz). The overlaid image of the POLI (peak SNR of 47) and QPI images show good agreement (Fig. 4(e)). Figure 4(f) shows the QPI image of the same cell for an exposure time of 10 ms.

## 5. Conclusions

This work demonstrates the use of low frequencies in a wide field POLI scheme yielding fast imaging with high SNR of 120. For comparison, in a preliminary effort an SNR of 18 was obtained using a phase-only wide field photothermal system [4]. Previously, an optical lock-in photothermal approach was combined with optical coherence microscopy (OCM) [5], producing 34dB SNR but requiring up to 5 seconds for image acquisition. There are two essential differences between the work presented here and the POLI-OCM approach. OCM operates in a backscattering configuration where the signal scales as the refractive index change ( $n$ ) while in transmission, the approach used here, the signal scales as the refractive index relative to the background ( $n-1$ ). The POLI-OCM system also conducts measurements in three dimensions with the POLI axial sectioning obtained by the confocal parameter of the imaging optics. Although this paper demonstrates only two-dimensional imaging, three dimensional sectioning could be obtained via z-scanning, with a comparable axial range imaged in a shorter acquisition time compared to this combined POLI-OCM based system. However, this was not a priority in this work since our nanoparticle tags were targeted to cell surface receptors. Another significant difference is that the POLI-OCM system and others employed higher modulation frequencies, on the order of hundreds of kHz [5,6,8,20], chosen to avoid the widening of the heated spot expected for lower modulation frequencies. In our case, modulation frequencies of a few hundred Hz resulted in a heated spot which is tens of micrometers in diameter (see Fig. 2 for example). However, in the case of cell imaging, heat diffusion is limited by the cell membrane. This results in the POLI signal being effectively localized to a given cell. Practically, this approach allows the identification of a tagged cell, confirming expression of a given receptor as was demonstrated in the cell imaging. To resolve the structure of the cell, the QPI mode of operation can be used. Thus, this combined imaging modality resolves cellular details (QPI) while also identifying NP-tagged cells (POLI). The ability of POLI to quickly and effectively identify cells with a particular receptor expression can be particularly useful in screening assays [21]. The wide field configuration

reduces the acquisition time to just 20 ms for live cells, while the low POLI modulation frequency opens the possibility to use simple instruments such as mechanical choppers for modulation of the signals.

### **Acknowledgments**

This work was supported by an NSF grant (MRI 1039562). WJE would like to acknowledge support from both the Chamber's Fellowship and the Pratt-Gardner Fellowship. AS would like to acknowledge support from the Rothschild Fellowship and the Weizmann Institute of Science - national postdoctoral award program for advancing women in science.